ARTICLE   OPEN

Magnetic states of coupled spin tubes with frustrated geometry in CsCrF$_4$

Masato Hagihala[1], Shohei Hayashida [1], Maxim Avdeev[2], Hirotaka Manaka[3], Hodaka Kikuchi[1] and Takatsugu Masuda [1]

When a theoretical model is realized in nature, small perturbation terms play important roles in the selection of the ground state in geometrically frustrated magnets. In case of a triangular spin tube, the two-dimensional network of the inter-tube interaction forms characteristic lattices. Among them Kagome-Triangular (KT) lattice is known to exhibit an enriched phase diagram including various types of non-trivial structures: non-coplanar cuboc structure, coplanar 120° structure with the two-dimensional propagation vector of $k_{2D} = (0, 0)$, $\sqrt{3} \times \sqrt{3}$ structure with $k_{2D} = (1/3, 1/3)$, and incommensurate structure. We investigate the magnetic state in the model material CsCrF$_4$ by using neutron diffraction technique. Combination of representation analysis and Rietveld refinement reveals that a very rare structure, i.e., a quasi-120° structure with $k_{2D} = (1/2, 0)$, is realized at the base temperature. The classical calculation of the phase diagram elucidates that CsCrF$_4$ is the first experimental realization of the KT lattice having ferromagnetic Kagome bond. A single-ion anisotropy and Dzyaloshinskii-Moriya interaction play key roles in the selection of the ground state. Furthermore, a successive phase transition having an intermediate state represented by $k_{2D} = (1/3, 1/3)$ is observed. The intermediate state is a partially ordered 120° structure which is induced by thermal fluctuation.

INTRODUCTION

Geometrical frustration in a magnetic material prevents the conventional Néel order and induces a non-trivial magnetic state at low temperatures. Particularly the two-dimensional (2D) triangular lattice has been extensively studied since the pioneering work on the quantum spin liquid in the Heisenberg antiferromagnet.[1] A consensus is that the ground state is the ordered state with 120° structure but is very close to quantum criticality.[2,3] In real compounds additional terms or perturbations such as anisotropy, further neighbor interaction, lattice distortion, etc., lift the macroscopic degeneracy of the ground state, and they lead to a variety of magnetic states.[4–8] Drastic changes caused by small perturbations in highly degenerated systems have attracted a lot of attention in condensed matter physics.

In one-dimensional (1D) systems quantum fluctuation as well as geometrical frustration induces non-trivial magnetic states. One of the examples is a frustrated triangular spin tube, where antiferromagnetic spins on triangular vertices are arrayed in one dimension. An early work on Heisenberg $S = 1/2$ spin tube reveals that the ground state is a dimerized non-magnetic state having a unit of a two-site rung singlet.[9] A finite energy gap in the magnetic dispersion and the exponential decay in spin correlation are predicted, and many theoretical studies have been reported so far.[10–16] Similar to the 2D systems, a small perturbation induces drastic change in the ground state.[17] Lattice distortion in the triangular rung breaks Z_2 symmetry, suppresses the spin gap, and induces a Tomonaga-Luttinger Liquid (TLL) state with vector chiral order.[18,19] In the classical Heisenberg system, on the other hand, a 120° structure is the ground state.
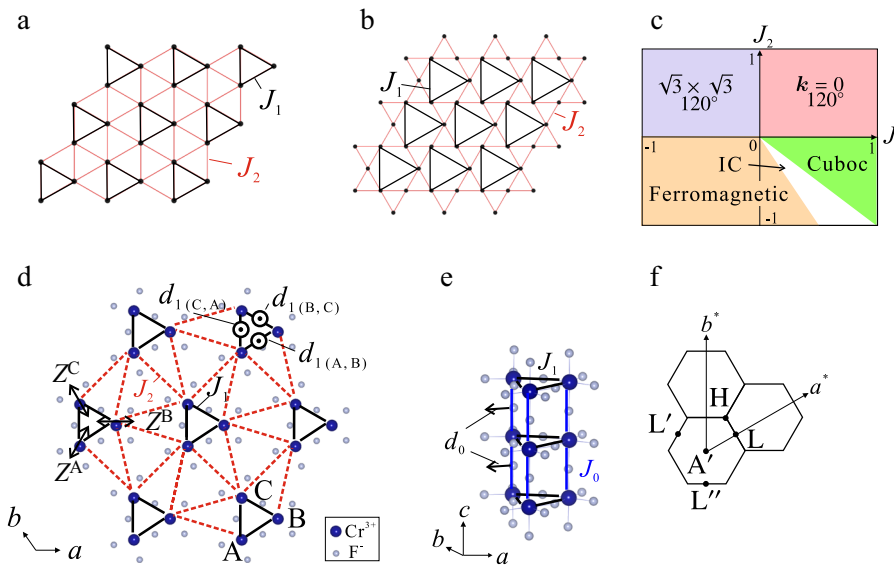
When the triangular spin tube is realized in nature, a geometry of the inter-tube interactions plays important roles. Particularly in the absences of frustration along the leg direction, the 2D-spin Hamiltonian in the plane perpendicular to the leg determines the spin structure. As an example of the tube configurations, supertriangular lattice in triangular lattice is shown in Fig. 1a. Here the triangular plaquettes are the cross sections of the tubes. The number of inter-triangular interactions of the lattice indicated by the red lines in Fig. 1a is four, which is the same as the coordination number in kagome lattice. In fact this supertriangular lattice can be transformed to Kagome-Triangular (KT) lattice[20] by reducing the length of the red lines as shown in Fig. 1b. Here nearest neighbor bond is J_2, which we will call *main Kagome bond* or simply *Kagome bond* hereafter, and the next-nearest neighbor (NNN) bond is J_1, which we will call *Triangular bond*. It is noted that two of four NNN interactions in the kagome lattice are effective. The lattice exhibits various phases in the $J_1 - J_2$ phase diagram as shown in Fig. 1c. The signs of J_is are positive for antiferromagnetic (AF) and negative for ferromagnetic (F), and the interaction is isotropic Heisenberg type. The predicted structures are non-coplanar cuboc, coplanar 120° with $k_{2D} = (0, 0)$, that with $k_{2D} = (1/3, 1/3)$, and incommensurate structures. Here the cuboc structure in the region of F-J_2 and AF-J_1 is a multi-Q structure having a 12-sublattice with the spins directing along the 12-middle points of a cube.[20–22] As far as we know, the reported magnetic structures of Kagome magnets in the absence of lattice distortion are threefold: (i) the 120° structure with $k_{2D} = (0, 0)$ in Fe and Cr-Jarosites,[23–28] the semimetals Mn$_3$Sn, Mn$_3$Ge,[29] and rare-earth tripod kagome,[30] (ii) the $\sqrt{3} \times \sqrt{3}$ structure with $k_{2D} = (1/3, 1/3)$ in high pressure phase in herbersmithite ZnCu$_3$(OH)$_6$Cl$_2$,[31] and (iii) the inplane ferromagnetic structure in V-Jarosite.[32] A material having F-J_2 and AF-J_1 which would exhibit non-trivial magnetic states has not been reported so far.

[1]Institute for Solid State Physics, University of Tokyo, Kashiwa, Chiba 277-8581, Japan; [2]Bragg Institute, Australian Nuclear Science and Technology Organization, Locked Bag 2001, Kirrawee DC NSW 2232, Australia and [3]Graduate School of Science and Engineering, Kagoshima University, Korimoto, Kagoshima 890-0065, Japan
Correspondence: Takatsugu Masuda (masuda@issp.u-tokyo.ac.jp)

Fig. 1 Introductory information on coupled spin tubes with frustrated geometry. **a** Geometry of the two-dimensional network of triangular spin tubes in the plane perpendicular to the leg: supertriangular lattice in triangular lattice **a**. **b** Kagome-Triangular (KT) lattice. J_1 is the Triangular bond and J_2 is the Kagome bond. **c** Phase diagram of the KT lattice [20]. **d**, **e** The crystal structure of CsCrF$_4$. Blue and small gray circles represent Cr^{3+} and F$^-$ ions, respectively. J_1 is the Triangular bond and J_2 is the Kagome bond. The $d_{1(\alpha,\beta)}$ is DM vector (α, β = A, B, C). z^A, z^B, and z^C are the z-axes locally defined on the Cr sites, A, B, and C. Spin tube runs along the c axis in **e**, and the tubes form the KT lattice in the $a-b$ plane in **d**. **f** High symmetry points in the 1st Brillouin zone of CsCrF$_4$ in the plane of (0 0 1/2)

The rare experimental realization of the equilateral triangular spin tube having the KT geometry is CsCrF$_4$.[33] The crystal structure is shown in Figs. 1d, e. Cr^{3+} ($3d^3$) ions, which are Jahn-Teller inactive and carry Heisenberg spins, form an equilateral triangular tube along the crystallographic c direction. The space group is $P\bar{6}2m$ with a hexagonal structure, and the lattice is free from distortion down to low temperatures. In the CrF$_6$ octahedron, the quasi-square of F$_4$ in the ab plane is slightly distorted to an isosceles trapezoid. The main origin of the magnetic interaction between Cr^{3+} ions is a super exchange interaction via F$^-$ ion. The angles of Cr-F-Cr for the rung direction is 148° and that for the chain direction is 180°, which indicate that both of the interaction along the leg J_0 and that along the rung J_1 are antiferromagnetic. The inter-tube interaction J_2 in the ab plane, which corresponds to the Kagome bond, is depicted by the dotted lines in Fig. 1e. The geometry is the same as that in Fig. 1a, meaning that the spin lattice is equivalent to the non-distorted KT lattice in Fig. 1b.[22]

The magnetic susceptibility of CsCrF$_4$ showed a broad maximum at $T \sim 60$ K, suggesting development of a short-range antiferromagnetic spin correlation.[34,35] Heat capacity showed no lambda-type anomaly above $T = 1.5$ K, and no clear evidence for a phase transition has been detected. The magnetic state was originally discussed in the context of the isolated spin tube. The heat capacity showed, however, a small bending around $T = 3$ K. Furthermore, a slight hysteresis was observed in the magnetic susceptibility between Zero Field Cooling (ZFC) and Field Cooling (FC) processes below $T = 5$ K. Broad peaks were observed for the linear and non-linear components of the AC susceptibility at 4 K and 3 K, respectively.[36] The details of the magnetic state of CsCrF$_4$ at low temperatures are, thus, complicated and unclear, and the frustrated two-dimensional geometry may have an important role.

In this paper, we demonstrate that non-trivial magnetic long-range ordered states are induced in CsCrF$_4$ which is a model compound of the KT lattice having the ferromagnetic Kagome bond by using neutron diffraction technique. Combination of the magnetic structure analysis and the calculation of the phase diagram reveals that a single-ion anisotropy and DM interaction select a very rare magnetic structure, i.e., quasi-120° structure with
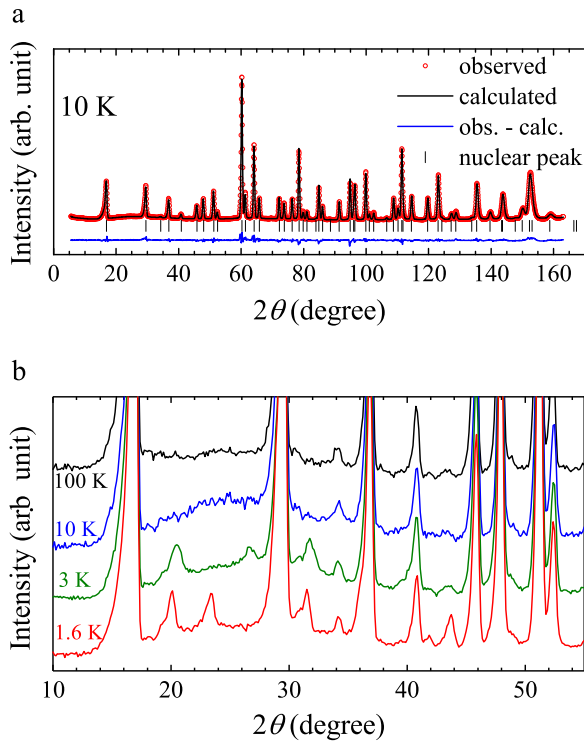
$\boldsymbol{k}_{2D} = (1/2, 0)$, at the base temperature. Furthermore, a successive phase transition is observed, and the intermediate temperature phase is partially ordered 120° structure.

RESULTS

Neutron diffraction
The neutron diffraction profiles at 10 K in Fig. 2a is reasonably reproduced by the calculation based on the crystal structure of CsCrF$_4$ previously reported in ref. [33]. The refined lattice parameters and atomic positions are summarized in Supplementary Note 2. As shown in Fig. 2b a broad peak is observed at $2\theta \sim 25°$, which corresponds to $Q \sim 1.2$ Å, at 10 K. The temperature is much lower than the maximum temperature (60 K) of the bulk susceptibility,[35] and the broad peak is ascribed to the development of magnetic short-range correlation. At 100 K, in contrast, the broad peaks is suppressed, and paramagnetic diffuse scattering exists in the small 2θ.
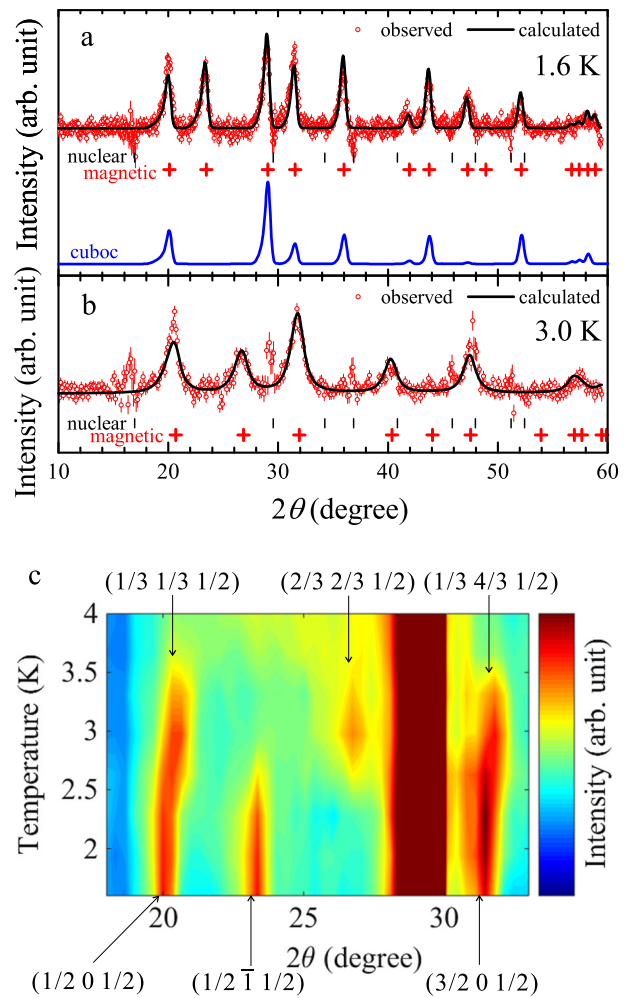
Figure 3a shows the diffraction profile obtained by subtracting the data at 10 K from that at 1.6 K. The details of the background subtraction are described in Supplementary Note 3. Well-defined peaks are observed, meaning that a magnetic order is realized. A spin liquid state that was originally supposed as the ground state[34,35] is, thus, not the case in CsCrF$_4$. Two-dimensional geometry of the inter-tube interaction is more important than the quantum nature of one-dimensional spin tube. We, hence, found that CsCrF$_4$ is an ideal model for the non-distorted KT lattice, where the main Kagome bond J_2 would be smaller than the Triangular bond J_1. The magnetic Bragg peaks are all indexed by (h k l) with h = half integer, k = integer, and l = half integer. The propagation vector is identified as $\boldsymbol{k}_1 = \left(\frac{1}{2}, 0, \frac{1}{2}\right)$ which coincides with the cuboc structure predicted in the KT lattice. This suggests that CsCrF$_4$ is a very rare experimental realization of the KT lattice having ferromagnetic Kagome bond. Figure 3b shows the subtracted profile measured at 3.0 K. The 2θs of the magnetic peaks are different from those measured at 1.6 K. The magnetic propagation vector is identified as $\boldsymbol{k}_2 = \left(\frac{1}{3}, \frac{1}{3}, \frac{1}{2}\right)$. The $\boldsymbol{k}_1$ and $\boldsymbol{k}_2$

Fig. 2 Neutron diffraction profiles. **a** Nuclear peak profile and the fitting to the data at 10 K. **b** Diffraction profiles at 100 K, 10 K, 3 K, and 1.6 K in the range of $2\theta = 10°–55°$

Fig. 3 Magnetic neutron diffraction profiles. **a, b** The magnetic diffraction profile at 1.6 K for **a** and that at 3.0 K for **b**. Fitting curve in **a** is based on the quasi-120° structure in Fig. 5a, and that in **b** is based on the partially ordered 120° structure in Fig. 5d. **c** The temperature variation of diffraction profiles in the range of $2\theta = 18°–33°$

coincide with high symmetry points in the first Brillouin zone, L and H in Fig. 1f, respectively.

The temperature evolution of the neutron profile without background subtraction in a heating process is shown in Fig. 3c. The variation of the 2θ positions of the magnetic peaks means a successive transition. Temperature dependences of the intensities of the magnetic Bragg peaks at $\left(\frac{1}{2}\bar{1}\frac{1}{2}\right)$ and $\left(\frac{2}{3}\frac{2}{3}\frac{1}{2}\right)$ are shown in Fig. 4a. The peak at $\left(\frac{1}{2}\bar{1}\frac{1}{2}\right)$ disappears at about $T_{N1} = 2.8$ K. We define the ordered phase at $T \leq T_{N1}$ as the low temperature (LT) phase. At $T \geq T_{N1}$ the peak at $\left(\frac{2}{3}\frac{2}{3}\frac{1}{2}\right)$ disappears at about $T_{N2} = 3.5$ K. We define the ordered phase at $T_{N1} \leq T \leq T_{N2}$ as the intermediate temperature (IT) phase. The diffuse scattering is suppressed below T_{N1} but still remains even at 1.6 K, which can be seen in Fig. 3c as well as Fig. 2b. The temperature dependences of the full width at half maximum (FWHM) of the peak of $\left(\frac{1}{2}2\frac{1}{2}\right)$ at $2\theta = 43.7°$ and $\left(\frac{4}{3}\frac{1}{3}\frac{1}{2}\right)$ at $2\theta = 31.7°$ are shown in Fig. 4b. The gray area is the experimental resolution estimated from the nuclear peak of (0 0 1) at 10 K. The dashed line is the FWHM of the peak, and the dotted lines are the errors for the FWHM. The FWHM of the peak at $\left(\frac{4}{3}\frac{1}{3}\frac{1}{2}\right)$ in the IT phase is wider than the resolution, meaning that the magnetic order in the IT phase is not truly long-ranged. The FWHMs at $\left(\frac{1}{2}2\frac{1}{2}\right)$ in the LT phase are much narrower than those in the IT phase, and they are resolution limited. Slight broadening at 2.4 K is ascribed to the uncertainty of the fitting. From the difference between the FWHM of the magnetic peak and the experimental resolution, the correlation length of the spins is estimated as a function of the temperature as shown in Fig. 4c. The maximum limit of the correlation length indicated by the dashed line is estimated as 800 Å. The correlation length gradually increases with the decrease of the temperature at $T_{N1} \leq T \leq T_{N2}$, and it is beyond the maximum limit at $T \leq T_{N1}$. The details of the estimate of FWHM and correlation length are described in Supplementary Notes 4 and 5, respectively.
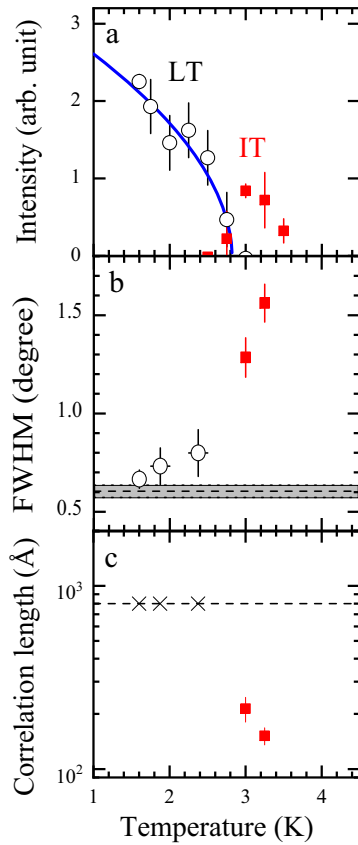
Magnetic structure analysis

The propagation vector of the LT phase is $\boldsymbol{k}_1 = \left(\frac{1}{2}, 0, \frac{1}{2}\right)$, and the scaler of the $\boldsymbol{k}_1$ coincides with that of the propagation vectors of the triple-k cuboc structure, $\boldsymbol{k}_1^1 = \left(\frac{1}{2}, 0, \frac{1}{2}\right)$, $\boldsymbol{k}_1^2 = \left(0, -\frac{1}{2}, \frac{1}{2}\right)$, and $\boldsymbol{k}_1^3 = \left(-\frac{1}{2}, \frac{1}{2}, \frac{1}{2}\right)$. Since the cuboc structure is predicted in Heisenberg KT lattice,[20] we simulate the neutron diffraction profile as shown in Fig. 2c. The calculated intensity at $\boldsymbol{q} = \left(\frac{1}{2}\bar{1}\frac{1}{2}\right)$ which corresponds to $2\theta = 23.5°$ is zero. In contrast, the magnetic peak is clearly observed. This means that the cuboc structure is not realized in $CsCrF_4$, suggesting that some additional perturbation terms are necessary. The detail of the cuboc structure is described in the Supplementary Note 6.

Next we construct spin models of single $\boldsymbol{k}$ structures. Irreducible representations (IRs) and their basis vectors that satisfy the space group $P\bar{6}2m$ and the propagation vector $\boldsymbol{k}_1 = \left(\frac{1}{2}, 0, \frac{1}{2}\right)$ are listed in Table 1. Because $\boldsymbol{k}_1$ breaks three-fold rotational symmetry of the hexagonal system, all the three Cr sites are not equivalent; the A and B sites are equivalent, but the C site is inequivalent. We assume that the magnetic structure in the LT phase is associated to a single IR.[37] We also assume that the magnitude of the moments on the Cr ions are the same. The candidates of the

Fig. 4 Temperature variations of magnetic Bragg peaks. **a** Temperature dependences of the intensities at (1/2 1̄ 1/2) (black circles) and (2/3 2/3 1/2) (red squares). **b** Temperature dependences of the full width at half maximum at (1/2 2 1/2) (black circles) and (4/3 1/3 1/2) (red squares). The gray area is the experimental resolution. **c** Temperature dependences of the correlation length of the IT phase estimated from the magnetic Bragg peaks at (4/3 1/3 1/2) (red squares). The dashed line is the maximum limit of the correlation length. The correlation lengths in the LT phase are beyond the limit, and the data are indicated by the black crosses

Table 1. The irreducible representations (IRs) and associated basis vectors (BVs) for the space group $P\bar{6}2m$ with k_1 on each Cr site

IR	BV	A site	B site	IR	BV	C site
Γ_1	ψ_1	(0, 0, −1)	(0, 0, 1)			
Γ_2	ψ_2	(−1, −1, 0)	(1, 0, 0)	Γ_2	ψ_7	(0, −1, 0)
	ψ_3	(0, 1, 0)	(0, 1, 0)			
Γ_3	ψ_4	(0, 0, 1)	(0, 0, 1)	Γ_3	ψ_8	(0, 0, 1)
Γ_4	ψ_5	(1, 1, 0)	(1, 0, 0)	Γ_4	ψ_9	$\left(\frac{2}{\sqrt{3}}, \frac{1}{\sqrt{3}}, 0\right)$
	ψ_6	(0, −1, 0)	(0, 1, 0)			

magnetic structures are, then, linear combinations of ψ_2, ψ_3, and ψ_7 for Γ_2, those of ψ_4 and ψ_8 for Γ_3, and those of ψ_5, ψ_6, and ψ_9 for Γ_4. In order to consider a high-symmetry structure, we first pick up 14 structures where the angles between the neighboring spins are fixed as 0°, 60°, 120° and 180° as listed in Table 2. The magnetic moments are expressed as follows;

$$\boldsymbol{m} = \frac{1}{2}\sum_i [C_i\psi_i \exp(-i(2\pi\boldsymbol{k}\cdot\boldsymbol{l}+\phi)) + c.c.] \qquad (1)$$

Rietveld analyses were performed on the models A_1–A_{14}, and the results are presented. The parameters of the crystal structure are fixed to those at 10 K. Furthermore, the angles between the spins are fixed, meaning that the ratios among C_i are fixed, and the number of the free parameters in the refinement is one. The reasonable agreement to the data was obtained for four 120° structures; A_2, A_5, A_{10} and A_{14}. To distinguish these 120° structures, we define vector chirality $\boldsymbol{\kappa}$ as follows;

$$\boldsymbol{\kappa} = \sum_{ijk} \frac{2}{3\sqrt{3}}\epsilon_{ijk}(\hat{\boldsymbol{m}}_i \times \hat{\boldsymbol{m}}_j), \qquad (2)$$

where i, j and k are assigned A, B or C, ϵ_{ijk} means Levi-Civita symbol, and $\hat{\boldsymbol{m}}_i$ is a magnetic moment normalized to 1. For the A_2 and A_{10} models $\kappa_c = 1$, and for the A_5 and A_{14} models $\kappa_c = -1$. Here κ_c is the c component of $\boldsymbol{\kappa}$. Next, we release the constraint of the angles between the neighboring spins, and we refined the coefficients of basis vectors for these four models. The results and the obtained models B_1–B_4 are shown in the lower panel in Table 2. The fitting indexes χ^2 and R_{wp} are improved, and among the models the B_1 and B_4 are better. For example the fitting curve for the model B_1 is indicated by the solid black curve in Fig. 3a. The fit to the data is good. ξ, ζ, and η in Table 2 are the angles of the moments on A and B sites, B and C sites, and C and A sites, respectively. We found that the models B_1 in Fig. 5a and B_4 in Fig. 5b, both of which are quasi-120° structures, are the final candidates of the magnetic structure in the LT phase in CsCrF$_4$. The moment sizes are about 1.4~1.5 μ_B for both candidates and they are considerably smaller than 3 μ_B, the full moment of Cr^{3+} ion. They are strongly fluctuated due to the geometrical frustration and the low dimensionality of the system. The details of the model fitting is described in Supplementary Note 3.

For the IT phase, due to broad widths of the magnetic Bragg peaks and large diffuse scattering, the peak profile could not be refined very accurately. Nevertheless, we performed Rietveld fit to the subtracted profile at 3 K on the basis of two models. One is $\sqrt{3}\times\sqrt{3}$ structure shown in Fig. 5c. The fit to the data is shown in the supplementary note, and it is reasonable. The estimated moment size is $m = 1.62(2)$ μ_B and the fitting quality are $\chi^2 = 2.15$ and $R_{wp} = 42.6$. It should be noted that the model is represented by 2 different IRs, Γ_2 and Γ_4 in Table 3. Another model is modulated all-in all-out structure as shown in Fig. 5d. This structure belongs to a single IR Γ_2 in Table 3. The fit to the data is shown by the solid black curve in Fig. 3b and it is reasonable. The magnitude of the estimated moment size is 2.49(3)μ_B, and the fitting quality are $\chi^2 = 1.72$ and $R_{wp} = 38.0$. The moment sizes of neighboring spins are expressed as $m\cos\phi$, $m\cos(\phi + 2/3\pi)$, $m\cos(\phi + 4/3\pi)$… Here the phase ϕ is arbitrary, and it cannot be determined by powder neutron diffraction.

Phase diagram

CsCrF$_4$ is originally a model material of the triangular spin tube, but the observation of the magnetic order in the present study reveals that the physics of the Kagome-Triangular (KT) lattice formed by the inter-tube interaction is important. Our analysis concluded that the LT phase is the quasi-120° structure at the L point in the first Brillouin zone, and the IT phase is $\sqrt{3}\times\sqrt{3}$ structure or modulated 120° structure at the H point. The LT structure is, however, different from the ground states expected in the Heisenberg KT lattice.[20] The expected cuboc structure and 120° structure with $\boldsymbol{k}=\boldsymbol{0}$ do not break three-fold rotational symmetry of the crystal. In contrast, the realized magnetic structure with $\boldsymbol{k} = \left(\frac{1}{2}, 0, \frac{1}{2}\right)$, which corresponds to $\boldsymbol{k}_{2D} = \left(\frac{1}{2}, 0\right)$, breaks the symmetry. Perturbation terms that induce the anisotropy, including DM interaction and/or single-ion anisotropy, are necessary. It is also noted that these terms stabilize a coplanar structure rather than a non-coplanar one. The magnitude of the

Table 2. Summary of Rietveld analyses

IR	Γ_2													
model	A$_1$		A$_2$		A$_3$		A$_4$		A$_5$			A$_6$		
BV	ψ_2	ψ_7	ψ_2	ψ_7	ψ_3	ψ_7	ψ_3	ψ_7	ψ_2	ψ_3	ψ_7	ψ_2	ψ_3	ψ_7
C_i	1.02(2)	1.02(2)	1.50(1)	−1.50(1)	1.17(2)	1.17(2)	0.78(2)	-0.78(2)	1.39(1)	1.39(1)	1.39(1)	1.06(2)	1.06(2)	-1.06(2)
χ^2	5.98		1.88		5.38		7.50		3.33			5.53		
R_{wp}	74.4		41.7		70.6		83.3		55.5			71.6		
κ_c	$-\frac{1}{3}$		1		0		0		-1			$\frac{1}{3}$		

IR	Γ_3				Γ_4								
model	A$_7$		A$_8$		A$_9$			A$_{10}$			A$_{11}$		
BV	ψ_4	ψ_8	ψ_4	ψ_8	ψ_5	ψ_6	ψ_9	ψ_5	ψ_6	ψ_9	ψ_5	ψ_6	ψ_9
C_i	1.04(3)	1.04(3)	1.26(2)	-1.26(2)	0.659(9)	1.32(2)	1.14(1)	0.737(9)	1.47(2)	-1.28(1)	1.04(2)	0.52(1)	0.90(2)
χ^2	8.09		5.35		4.49			3.62			6.44		
R_{wp}	86.5		70.4		64.5			57.9			77.2		
κ_c	0		0		$-\frac{1}{3}$			1			0		

IR	Γ_4								
model	A$_{12}$			A$_{13}$			A$_{14}$		
BV	ψ_5	ψ_6	ψ_9	ψ_5	ψ_6	ψ_9	ψ_5	ψ_6	ψ_9
C_i	1.02(2)	0.51(1)	-0.89(2)	0.633(9)	-0.633(9)	1.10(2)	0.776(7)	-0.776(7)	-1.34(1)
χ^2	7.20			5.05			2.73		
R_{wp}	81.6			68.4			50.3		
κ_c	0			$-\frac{1}{3}$			-1		

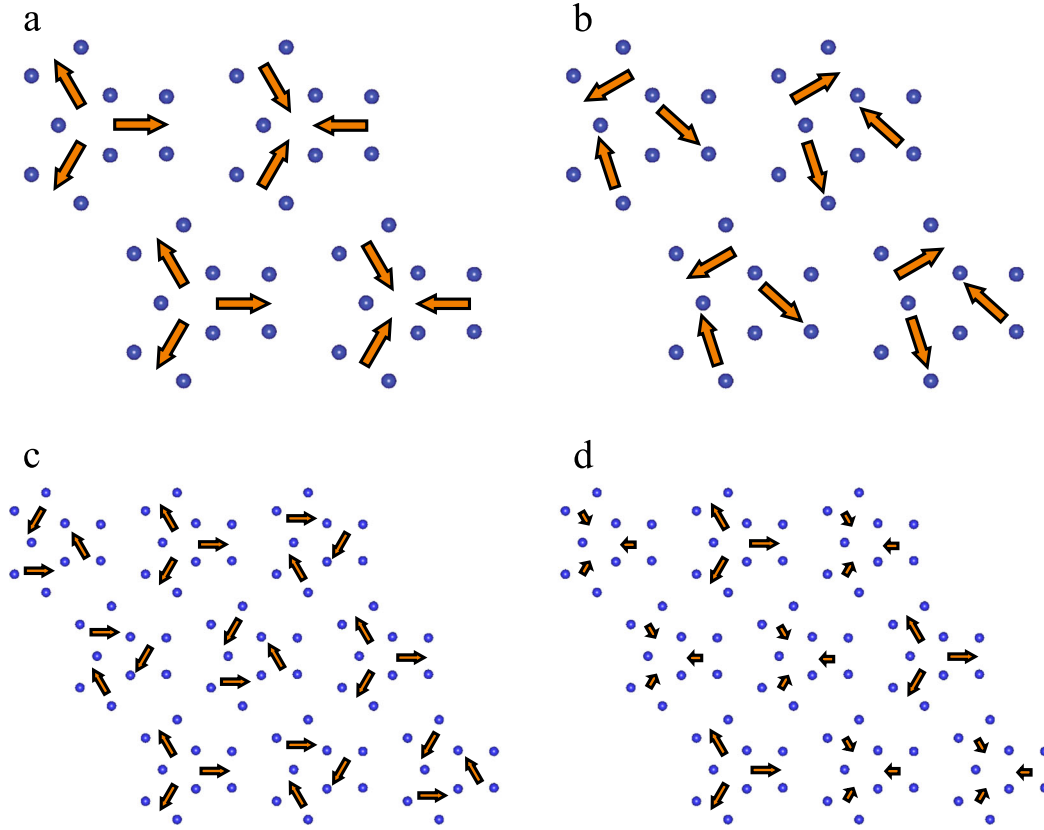| IR	Γ_2						Γ_4					
model	B$_1$			B$_2$			B$_3$			B$_4$		
BV	ψ_2	ψ_3	ψ_7	ψ_2	ψ_3	ψ_7	ψ_5	ψ_6	ψ_9	ψ_5	ψ_6	ψ_9
C_i	1.51(2)	0.02(3)	-1.50(1)	1.32(2)	1.45(2)	-1.39(1)	0.59(2)	1.478(8)	-0.744(8)	0.49(2)	-1.076(9)	0.802(6)
m (μ_B)	1.50(1)			1.39(1)			1.29(1)			1.39(1)		
ζ, η (deg.)	119.5(7)			124(1)			114(1)			108(1)		
ξ (deg.)	121(2)			111(2)			133(2)			144(2)		
χ^2	1.88			3.29			3.50			2.19		
R_{wp}	41.7			55.1			56.9			45.0		
κ_c	1.000(5)			-0.994(7)			0.988(8)			-0.952(7)		
comment	from A$_2$			from A$_5$			from A$_{10}$			from A$_{14}$		

Upper three panels show the results of Rietveld analyses for high-symmetry models A$_1$–A$_{14}$, where the constraint is imposed on the angle between the spins. The models A$_2$, A$_5$, A$_{10}$, and A$_{14}$ give better χ^2 and R_{wp}. The R_e of all the models are 30.4. Lower panel shows the results of the refinement of the better four models. The C_i is a coefficient value of the basis vector described in Eq. (2). The ξ, ζ and η in the lower panel are the angles between the spins on A and B-sites, those on B and C-sites, and those on C and A-sites, respectively

DM vectors for both tube's leg and rung are expected to be as small as 1–2% of the exchange interaction.[36] Nevertheless, the main kagome bond J_2, which has the exchange path of $Cr^{3+}−F^−−F^−−Cr^{3+}$, is also small, and the perturbation terms can be comparable to J_2. The perturbation terms as well as J_2 are, thus, important for the selection of the ground state.

We classically calculated phase diagrams of the ground state of $CsCrF_4$ using Luttinger-Tisza method.[38,39] The Hamiltonian is as

Fig. 5 Candidates of the magnetic structures of CsCrF$_4$. The blue circles are F ions and the arrows are the spins on Cr ions. **a, b** The magnetic structures in the LT phase proposed from the analysis. The structure in **b** is rejected after the discussion on the phase diagram in Fig. 4. **c, d** Candidates in the IT phase

Table 3. The irreducible representations (IRs) and associated basis vectors (BVs) for the space group $P\bar{6}2m$ with k_2 on each Cr site

IR	BV	A site	B site	C site
Γ_2	ψ_1	$(-1, -1, 0)$	$(1, 0, 0)$	$(0, 1, 0)$
Γ_3	ψ_2	$(0, 0, 1)$	$(0, 0, 1)$	$(0, 0, 1)$
Γ_4	ψ_3	$\left(\frac{1}{\sqrt{3}}, -\frac{1}{\sqrt{3}}, 0\right)$	$\left(\frac{1}{\sqrt{3}}, -\frac{2}{\sqrt{3}}, 0\right)$	$\left(-\frac{2}{\sqrt{3}}, -\frac{1}{\sqrt{3}}, 0\right)$
Γ_5	ψ_4	$\left(0, 0, \frac{-1+\sqrt{3}i}{2}\right)$	$(0, 0, 1)$	$\left(0, 0, \frac{-1-\sqrt{3}i}{2}\right)$
	ψ_5	$\left(0, 0, \frac{1+\sqrt{3}i}{2}\right)$	$\left(0, 0, \frac{1+\sqrt{3}i}{2}\right)$	$(0, 0, -1)$
Γ_6	ψ_6	$\left(\frac{1-\sqrt{3}i}{2}, \frac{1-\sqrt{3}i}{2}, 0\right)$	$(1, 0, 0)$	$\left(0, \frac{-1-\sqrt{3}i}{2}, 0\right)$
	ψ_7	$\left(\frac{-1+\sqrt{3}i}{2}, 0, 0\right)$	$(0, 1, 0)$	$\left(\frac{1+\sqrt{3}i}{2}, \frac{1+\sqrt{3}i}{2}, 0\right)$
	ψ_8	$\left(\frac{1-\sqrt{3}i}{2}, \frac{1-\sqrt{3}i}{2}, 0\right)$	$\left(\frac{-1-\sqrt{3}i}{2}, 0, 0\right)$	$(0, 1, 0)$
	ψ_9	$\left(0, \frac{-1+\sqrt{3}i}{2}, 0\right)$	$\left(\frac{1+\sqrt{3}i}{2}, \frac{1+\sqrt{3}i}{2}, 0\right)$	$(1, 0, 0)$

follows;

$$\mathcal{H} = \sum_{\mathbf{l}_\alpha, \mathbf{l}_\beta, \mathbf{l}'_\beta} \left(J_0 \mathbf{S}(\mathbf{l}_\alpha) \cdot \mathbf{S}(\mathbf{l}_\alpha + \mathbf{c}) + J_1 \mathbf{S}(\mathbf{l}_\alpha) \cdot \mathbf{S}(\mathbf{l}_\beta) \right. \tag{3}$$
$$\left. + J_2 \mathbf{S}(\mathbf{l}_\alpha) \cdot \mathbf{S}(\mathbf{l}'_\beta) + \mathbf{d}_{1(\alpha,\beta)} \cdot \mathbf{S}(\mathbf{l}_\alpha) \times \mathbf{S}(\mathbf{l}_\beta) + D(\mathbf{S}^{z^\alpha}(\mathbf{l}_\alpha))^2 \right).$$

Here $\mathbf{l}_\alpha$ is the position vector at α-site ($\alpha = $ A, B, and C) in the lattice $\mathbf{l}$, and $\mathbf{c}$ is the unit vector of the crystal lattice along the c

direction. z^α is the local z-axis defined at the α-site as shown in Fig. 1e. The sum is taken for $\mathbf{l}_\alpha$, $\mathbf{l}_\beta$, and $\mathbf{l}'_\beta$ all over the crystal, where $\alpha \neq \beta$ and $\mathbf{l} \neq \mathbf{l}'$. The schematic exchange pathways are shown in Figs. 1d, e. J_0 and J_1 are the exchange interactions of the tube's leg and rung, respectively. J_2 is the inter-tube interaction. The DM vector in the middle of the rung is $\mathbf{d}_1$, and it is along the c axis.[36] The directions of the $\mathbf{d}_1$s are not determined but they are all up or all down. The DM vector in the middle of the leg $\mathbf{d}_0$ is also allowed in the crystallographic symmetry. $\mathbf{d}_0$, however, induces an incommensurate spin correlation along the c direction, which is not the case in CsCrF$_4$. We, hence, ignore $\mathbf{d}_0$ in our calculation. Another additional term, single-ion anisotropy D, is also considered. The easy axes are assumed as the locally defined z^α-axes ($\alpha = $ A, B, C) as shown in Fig. 1d so that the anisotropy terms preserve three-fold rotational symmetry in the ab plane. The fixed values of J_0 and J_1 are used; $J_1 = 0.5$ and $J_0 = 1$.[40] In the calculation the J_2, d_1 and D are much smaller than J_0 and J_1, since Cr^{3+} ion is isotropic and the bond length of J_2 is long. The Hamiltonian in Eq. (3) is transformed into the wave vector space, and the eigenstates and eigenenergies are obtained by the diagonalization. The propagation vector of the ground state is obtained as the wave vector $\mathbf{k}$ that gives the minimum eigenenergy. The magnetic structure is obtained from the corresponding eigenstate.[38,39] A constraint that the magnitude of the spins are the same was imposed.

Figure 6a shows the d_1-J_2 phase diagram in the absence of the single-ion anisotropy D. When J_2 is AF, i.e., $J_2 > 0$, the ground state is 120° structure with $\mathbf{k} = \left(0, 0, \frac{1}{2}\right)$, which we call the A′ structure (red symbols). The propagation vector corresponds to $\mathbf{k}_{2D} = (0, 0)$ in the ab plane. On the other hand, when J_2 is FM the cuboc

Fig. 6 The phase diagram of $CsCrF_4$ calculated by Luttinger-Tisza method. d_1 is the magnitude of the DM interaction, D is the single-ion anisotropy on the Cr-site, and J_2 is the inter-tube interaction. **a** d_1-J_2 phase diagram in the absence of D. **b-d** $D-J_2$ phase diagrams for $d_1 = 0$, -0.01, and 0.01

structure (green squares) exists even at very small J_2 for $|d_1| = 0$. The DM interaction stabilizes a coplanar structure in the ab plane and destabilizes the cuboc structure. Indeed, at large $|d_1|$ coplanar $\sqrt{3} \times \sqrt{3}$ structures with $\boldsymbol{k} = \left(\frac{1}{3}, \frac{1}{3}, \frac{1}{2}\right)$ or $\boldsymbol{k}_{2D} = \left(\frac{1}{3}, \frac{1}{3}\right)$, which we call the H structures (blue symbols), appears. Positive d_1 induces negative chirality and negative d_1 induces positive chirality for both A′ and H structures. In this phase diagram, the single-k 120° structure with $\boldsymbol{k} = \left(\frac{1}{2}, 0, \frac{1}{2}\right)$ which is realized in $CsCrF_4$, does not exist.

Introduction of the single-ion anisotropy suppresses the non-coplanar cuboc structure and induces the single-k quasi-120° structure (orange symbols) in the range of $J_2 < 0$, which we call the L structure, as shown in the $D-J_2$ phase diagrams for $d_1 = 0$ and -0.01 (Figs. 6b, c). The propagation vector is $\boldsymbol{k} = \left(\frac{1}{2}, 0, \frac{1}{2}\right)$ or $\boldsymbol{k}_{2D} = \left(\frac{1}{2}, 0\right)$, and the magnetic unit cell in the ab plane is doubled along the a direction. Because of the geometry of the easy axis, all-in all-out structure with the positive chirality, which is one of the candidates of the magnetic structure in the LT phase in Fig. 5a, is realized. In Fig. 6c the H structure with positive chirality, which

coincides with a candidate in the IT phase in Fig. 5c, exists at small D. For $d_1 = 0.01$, the DM interaction favoring negative chirality and the single-ion anisotropy favoring positive chirality compete to each other. The H structure with negative chirality exists in wide region, and the strong single-ion anisotropy induces the L structure indicated by the model A_5 in Table 2. This magnetic structure is different from another candidate having negative chirality in the LT phase proposed by the experiment shown in Fig. 5b. For both cases where $d_1 = \pm 0.01$, 120° structure with $\boldsymbol{k}_{2D} = (0, 0)$ is stable.

The triangle in the L structures in Figs. 6b–d is distorted due to J_2. It is, however, small; the most distorted case in the range of our calculation is that the angles between the neighboring spins are $\zeta = \eta = 117°$ and $\xi = 127°$ at $J_2 = -0.03$, $D = -0.02$, and $d_1 = -0.01$.

DISCUSSION

One of the candidates for the magnetic structure of $CsCrF_4$ in the LT phase is the L structure with positive chirality as shown in Fig. 5a. The appearance of the structure requires ferromagnetic Kagome bond J_2 and single-ion anisotropy, and the DM interaction enhances the region of the structure in the $D - J_2$ phase diagrams as shown in Figs. 6b, c. Another candidate, the L structure having negative chirality, is shown in Fig. 5b. The structure is, however, does not exist in our phase diagram. We, therefore, reject the candidate, and conclude that the all-in all-out structure in Fig. 5a is realized in the LT phase. The conclusion means that $CsCrF_4$ is a rare experimental realization of the distortion free KT lattice having ferromagnetic Kagome bond.

Here we discuss the origin of the successive transition and the IT phase. The phase of the H structure and that of the L structure phase are adjacent in Fig. 6c. Suppose that $CsCrF_4$ is in the H structure and in the vicinity of the phase boundary. Since the H structure covers the region of $|D| < |d_1|$ in the phase diagram of the ground state, at finite temperatures of $|D| < k_B T < |d_1|$, the L structure is suppressed due to the thermal fluctuation, and the H structure is enhanced. This is a possible explanation for the appearance of the IT phase and the successive transition in $CsCrF_4$.

The $\sqrt{3} \times \sqrt{3}$ structure in the H structure is, however, represented by two different IRs, Γ_2 and Γ_4, and its realization contradicts conventional Landau theory for second order phase transition. In this sense, the modulated all-in all-out structure in Fig. 5d is represented by the single IR Γ_2 in Table 3, and its realization is more reasonable. This modulated structure is regarded that the spins component of the easy-axis direction in the $\sqrt{3} \times \sqrt{3}$ structure in Fig. 5c is statically ordered. The partially ordered 120° structure is, thus, more reasonable for the IT phase in the successive transition.

We discuss the reason why lambda-type anomaly was not observed in the heat capacity,[34] even though the magnetic ordered state is realized. As shown in Fig. 2b, the strong magnetic diffuse scattering was observed at 10 K. This suggests that the short-range correlation of the spins is developed, and considerable amount of the magnetic entropy is consumed already at $T > T_{N2}$. At $T \leq T_{N2}$ in the IT phase, the magnetic diffuse scattering still remains. The result means that the entropy change at T_{N2} is small. At $T_{N1} \leq T \leq T_{N2}$ the spin correlation is not long-ranged, and the correlation length gradually changes with the decrease of the temperature. The change of the entropy is, thus, smeared in wide temperature range in $CsCrF_4$, and the sharp anomaly was not detected in the heat capacity measurement.

Finally it should be noted that the threshold for the long-range order is determined by the experimental resolution, and, therefore, the possibility of short-range order with the correlation length longer than 800 Å cannot be excluded for the LT phase at $T \leq T_{N1}$. In addition the dynamical spin correlation is not measured in the present neutron diffraction experiment. Possible short-

range correlations in space and time in the LT phase also smears the change of the entropy.

In summary, we identified the magnetic states at low temperatures in a model material of triangular spin tubes coupled by the inter-tube interaction having KT geometry $CsCrF_4$. Magnetically ordered state was observed in contrast with previous studies. The quasi-120° structure with $\boldsymbol{k}_{2D} = (1/2, 0)$, which has not been predicted in theory in the category of the kagome lattice magnets, was experimentally identified. Single-ion anisotropy and DM interaction play important role for the selection of the magnetic structure. A successive phase transition was observed, and the magnetic structure in the IT phase is partially ordered 120° structure represented by $\boldsymbol{k}_{2D} = (1/3, 1/3)$. The IT phase is reasonably explained under the assumption that $CsCrF_4$ is in the vicinity of the phase boundary in the $D - J_2$ phase diagram. Since the key parameters, J_2, D, and d_1, are small in $CsCrF_4$, they can be controlled by, for example, pressure in extensive scales. In the system where a perturbation term has a casting vote for the selection of the state, external parameters including temperature, pressure, and magnetic field can induce various types of magnetic states. Further study in the wide range in the phase space will open a new window for the search of novel state of matter.

METHODS

High quality polycrystalline sample with the mass of 10 g was prepared by the solid state reaction method.[34,35] The quality of the sample is discussed in the Supplementary Note 1. Lambda-type anomaly was not observed in the heat capacity measurement on the sample with the same quality as that used for neutron scattering experiment. Neutron diffraction experiments were carried out by the use of the powder neutron spectrometer ECHIDNA installed in the research reactor OPAL at ANSTO. Ge(331) monochromator was used and the neutron wavelength was $\lambda = 2.4395$ Å. The coverage of the scattering angle was $6° \leq 2\theta \leq 165°$. The measurement temperatures were $T = 1.6$ K, 1.75 K–3.5 K at intervals of 0.25 K, 4 K, 10 K and 100 K. A conventional liquid He cryostat was used to achieve the low temperatures. The Rietveld analysis was performed using the FULLPROF software package.[41] To consider the candidates for the magnetic structure on the basis of the crystallographic space group and the magnetic propagation vector, the group theory method was used. Irreducible representations (IRs) were calculated using BasIreps in FullProf Suite.

DATA AVAILABILITY

The data that support the findings of this study are available from the corresponding author upon reasonable request.

AUTHOR CONTRIBUTIONS

T.M. initiated and supervised the project. M.H. and T.M. wrote the manuscript. S.H. and H.K. joined in the discussion. M.A. performed neutron diffraction experiment. H.M. synthesize the sample. All the co-authors discussed the results and improved manuscript.

ADDITIONAL INFORMATION

Supplementary information accompanies the paper on the npj Quantum Materials website (https://doi.org/10.1038/s41535-019-0152-5).

Competing interests: The authors declare no competing interests.

Publisher's note: Springer Nature remains neutral with regard to jurisdictional claims in published maps and institutional affiliations.

REFERENCES

1. Anderson, P. W. Resonating valence bonds: a new kind of insulator? Mat. Res. Bull. **8**, 153–160 (1973).
2. Singh, R. R. P. & Huse, D. A. 3-sublattice order in triangular-lattice and kagome-lattice spin-half antiferromagnets. Phys. Rev. Lett. **68**, 1766–1769 (1992).
3. Bernu, B., Lecheminant, P., Lhuillier, C. & Pierre, L. Exact spectra, spin susceptibilities, and order parameter of the quantum Heisenberg antiferromagnet on the triangular lattice. Phys. Rev. B **50**, 10048–10063 (1994).
4. Mekata, M. & Adachi, K. Magnetic-structure of $CsCoCl_3$. J. Phys. Soc. Jpn. **44**, 806–812 (1978).
5. Zhou, H. D. et al. Successive phase transitions and extended spin-excitation continuum in the $S = 1/2$ triangular-lattice antiferromagnet $Ba_3CoSb_2O_9$. Phys. Rev. Lett. **109**, 267206 (2012).
6. Yamashita, S. et al. Thermodynamic properties of a spin-1/2 spin-liquid state in a κ-type organic salt. Nat. Phys. **4**, 459–462 (2008).
7. Itou, T., Oyamada, A., Maegawa, S. & Kato, R. Instability of a quantum spin liquid in an organic triangular-lattice antiferromagnet. Nat. Phys. **6**, 673–676 (2010).
8. Miyashita, S. & Kawamura, H. Phase-transitions of anisotropic Heisenberg antiferromagnets on the triangular lattice. J. Phys. Soc. Jpn. **54**, 3385–3395 (1985).
9. Kawano, K. & Takahashi, M. Three-leg antiferromagnetic Heisenberg ladder with frustrated boundary condition; Ground state properties. J. Phys. Soc. Jpn. **66**, 4001–4008 (1997).
10. Wang, H.-T. Elementary excitations in the spin-tube and spin-orbit models. Phys. Rev. B **64**, 174410 (2001).
11. Lüscher, A., Noack, R. M., Misguich, G., Kotov, V. N. & Mila, F. Soliton binding and low-lying singlets in frustrated odd-legged $S = 1/2$ spin tubes. Phys. Rev. B **70**, 060405 (2004).
12. Sato, M. & Sakai, T. Vector chirality and inhomogeneous magnetization in frustrated spin tubes in high magnetic fields. Phys. Rev. B **75**, 014411 (2007).
13. Schmidt, H.-J. & Richter, J. Exact ground states for coupled spin trimers. J. Phys. A Math. Theor. **43**, 405205 (2010).
14. Sakai, T., Sato, M., Okamoto, K., Okunishi, K. & Itoi, C. Quantum spin nanotubes-frustration, competing orders and criticalities. J. Phys. Condens. Matter **22**, 403201 (2010).
15. Nishimoto, S., Fuji, Y. & Ohta, Y. Spin gap of the three-leg $S = 3/2$ Heisenberg tube. Phys. Rev. B **83**, 224425 (2011).
16. Lajkó, M., Sindzingre, P. & Penc, K. Exact ground states with deconfined gapless excitations for the three-leg spin-1/2 tube. Phys. Rev. Lett. **108**, 017205 (2012).
17. Nishimoto, S. & Arikawa, M. Low-lying excitations of the three-leg spin tube: A density-matrix renormalization group study. Phys. Rev. B **78**, 054421 (2008).
18. Sato, M. Coexistence of vector chiral order and Tomonaga-Luttinger liquid in the frustrated three-leg spin tube in a magnetic field. Phys. Rev. B **75**, 174407 (2007).
19. Sakai, T. et al. Quantum phase transitions of the asymmetric three-leg spin tube. Phys. Rev. B **78**, 184415 (2008).
20. Ishikawa, H., Okubo, T., Okamoto, Y. & Hiroi, Z. Kagome-Triangular lattice antiferromagnet $NaBa_2Mn_3F_{11}$. J. Phys. Soc. Jpn. **83**, 043703 (2014).
21. Domenge, J.-C., Sindzingre, P., Lhuillier, C. & Pierre, L. Twelve sublattice ordered phase in the J_1-J_2 model on the kagome lattice. Phys. Rev. B **72**, 024433 (2005).
22. Seki, K. & Okunishi, K. Magnetic phase diagram of the coupled triangular spin tubes for $CsCrF_4$. Phys. Rev. B **91**, 224403 (2015).
23. Inami, T., Nishiyama, M., Maegawa, S. & Oka, Y. Magnetic structure of the kagome lattice antiferromagnet potassium jarosite $KFe_3(OH)_6(SO_4)_2$. Phys. Rev. B **61**, 12181–12186 (2000).
24. Wills, A. S. Long-range ordering and representational analysis of the jarosites. Phys. Rev. B **63**, 064430 (2001).
25. Wills, A. S., Harrison, A., Ritter, C. & Smith, R. I. Magnetic properties of pure and diamagnetically doped jarosites: Model kagomé antiferromagnets with variable coverage of the magnetic lattice. Phys. Rev. B **61**, 6156–6169 (2000).
26. Grohol, D., Nocera, D. G. & Papoutsakis, D. Magnetism of pure iron jarosites. Phys. Rev. B **67**, 064401 (2003).
27. Inami, T. et al. Magnetic ordering in the kagome lattice antiferromagnet $KCr_3(OD)_6(SO_4)_2$. Phys. Rev. B **64**, 054421 (2001).
28. Scheie, A. et al. Effective spin-1/2 scalar chiral order on kagome lattices in $Nd_3Sb_3Mg_2O_{14}$. Phys. Rev. B **93**, 180407(R) (2016).
29. Nagamiya, T., Tomiyoshi, S. & Yamaguchi, Y. Triangular spin configuration and weak ferromagnetism of Mn_3Sn and Mn_3Ge. Solid State Commun. **42**, 385–388 (1982).
30. Dun, Z. L. et al. Magnetic ground states of the rare-earth tripod Kagome lattice $Mg_2RE_3Sb_3O_{14}$ (RE = Gd, Dy, Er). Phys. Rev. Lett. **116**, 157201 (2016).

31. Kozlenko, D. P. et al. From quantum disorder to magnetic order in an $s = 1/2$ Kagome lattice: a structural and magnetic study of Herbertsmithite at high pressure. *Phys. Rev. Lett.* **108**, 187207 (2012).

32. Grohol, D. et al. Powder neutron diffraction analysis and magnetic structure of kagomé-type vanadium jarosite $NaV_3(OD)_6(SO_4)_2$. *Phys. Rev. B* **68**, 094404 (2003).

33. Babel, V. D. & Knoke, G. Structures of fluorides with caesium. IV. The crystal structure of $CsCrF_4$ a novel tetrafluorometallate type with chain structure. *Z. Anorg. Allg. Chem.* **442**, 151–162 (1978).

34. Manaka, H. et al. Spin-liquid state study of equilateral triangle $S = 3/2$ spin tubes formed in $CsCrF_4$. *J. Phys. Soc. Jpn.* **78**, 093701 (2009).

35. Manaka, H. et al. Effects of geometrical spin frustration on triangular spin tubes formed in $CsCrF_4$ and α-$KCrF_4$. *J. Phys. Soc. Jpn.* **80**, 084714 (2011).

36. Manaka, H. & Miura, Y. Spin dynamics of triangular spin tubes. *J. Korean Phys. Soc.* **62**, 2032–2036 (2013).

37. Izyumov, Yu. A. & Naish, V. E. Symmetry analysis in neutron diffraction studies of magnetic structures: 1. A phase transition concept to describe magnetic structures in crystals. *J. Mag. Mag. Mat.* **12**, 239–248 (1979).

38. Luttinger, J. M. & Tisza, L. Theory of dipole interaction in crystals. *Phys. Rev.* **70**, 954 (1946).

39. Kaplan, T. A. & Menyuk, N. Spin ordering in three-dimensional crystals with strong competing exchange interactions. *Philos. Mag.* **87**, 3711–3785 (2006).

40. Koo, H.-J. On the cause for the no spin-gap behavior of the triangular spin tube system $CsCrF_4$. *J. Mag. Mag. Mat.* **324**, 2806–2808 (2012).

41. Rodríguez-Carvajal, J. Recent advances in magnetic structure determination by neutron powder diffraction. *Phys. B* **192**, 55–69 (1993).